Article:
Cai, N, Xia, S, Li, X et al. (7 more authors) (2021) High-value products from ex-situ catalytic pyrolysis of polypropylene waste using iron-based catalysts: the influence of support materials. Waste Management, 136. pp. 47-56. ISSN 0956-053X

https://doi.org/10.1016/j.wasman.2021.09.030

High-value products from ex-situ catalytic pyrolysis of polypropylene waste using iron-based catalysts: the influenceof support materials

Ning Cai[1], Sunwen Xia [1],Xiaoqiang Li[1],Haoyu Xiao[1], Xu Chen[1],Yingquan Chen[1*], Pietro Bartocci[2], Hanping Chen[1], Paul T. Williams[3], Haiping Yang[1]*

[1]*State Key Laboratory of Coal Combustion, School of Energy and Power Engineering, Huazhong University of Science and Technology, 430074, Wuhan, PR China*

[2]*Department of Engineering, University of Perugia, via G. Duranti 67, 06125, Perugia, Italy*

[3]*School of Chemical and Process Engineering, University of Leeds, Leeds, LS2 9JT UK*

**Correspondingauthor;*

Email addresses: chenyingquan@hust.edu.cn (Y. Chen),yhping2002@163.com (H, Yang)

Abstract: Catalytic pyrolysisis considered a promising strategy for the utilisation of plastic waste from the economic and environmental perspectives. As such, the supporting materials play a critical role in the properties of the catalyst. This study clarified this influence onthe dispersion of the iron (Fe) within an experimental context. Four different types of typical supports with different physical structures were introduced and explored in a two-stage fixed-bed reactor; these included metallic oxides (Al_2O_3, TiO_2), a non-metallic oxide (SiO_2), and molecular sieves (ZSM-5). The results show that the liquid products were converted into carbon deposits and lighter gaseous products, such as hydrogen. The Al_2O_3-supported catalyst with a relatively moderate specific surface areas and average pore diameter exhibited improved metal distribution with higher catalytic activity. In comparison, the relatively low specific surface areas of TiO_2 and small average pore diameters of ZSM-5 had a negative impact on metal distribution and the subsequent catalytic reformation process; this wasbecause of the inadequate reaction during the catalytic process. The Fe/Al_2O_3 catalyst produced ahigher yield of carbon deposits (30.2 wt.%), including over 65% high-value carbon nanotubes (CNTs) and hydrogen content (58.7 vol.%). Additionally,

more dispersive and uniform CNTs were obtained from the Fe/SiO_2 catalyst. The Fe/TiO_2 catalyst promoted the formation of carbon fibre twisted like fried dough twist. Notably, there was interesting correspondence between the size of the reduced Fe nanoparticles and the product distribution. Within certain limits, the smaller Fe particle size facilitatesthecatalytic activity. The smaller and better dispersed Fe particles over the support materials were observed to be essential for hydrocarbon cracking and the subsequent formation of carbon deposits.The findings from this study may provide specific guidance for the preparation of different forms of carbon materials.

Keywords： Waste plastics;Catalytic pyrolysis; Support materials;Hydrogen; Carbon nanotubes

1 Introduction

With the advancement of the modern society, polymer plasticsare well-received owing to their superior performance and are widely used in industry and production. However, many plasticshave a short longevity and tend to become part of the municipal solid waste (MSW) stream(Li et al., 2020b). In 2017, approximately8.3 billion tons of plastic waste was generated worldwide;only 9wt.% of this waste was recycled(Geyer et al., 2017). The onset of the novel coronavirus (COVID-19) pandemic has rapidly increased the consumption of plasticssuch as personal protective equipment (PPE) (Prata et al., 2020). Therefore, the recovery of the plastic wastefor the manufacture of high-value products is of great significance and has been attracting increasing attention.

Compared with traditional incineration or landfilling, catalytic pyrolysisis considered as an efficient meansto convertwaste plastic into high-value products such as hydrogen (Williams et al., 2020; Yao et al., 2017), jet fuel (Huo et al., 2020; Zhang et al., 2019) and carbon nanotubes(CNTs)(Nahil et al., 2015; Williams et al., 2020). As such, catalytic pyrolysis has demonstrated enormous potential for plastic waste recovery and utilisationas it creates valuable products while reducing environmental pollution (Ellis et al., 2021). Moreover, naphtha may be a promising means to recycle polyolefins for the development of a circular economy (Dai et al., 2021). Based on the requirementsof cracking carbon–carbon and carbon–hydrogen bonds, transition metal (iron and nickel)based catalysts have been broadly used in the catalytic pyrolysis of plasticwaste (Ahmed et al., 2009; Jonathan et al., 2016; Wang et al., 2020a). Acombet al. (Acomb et al., 2013)investigated thecatalytic pyrolysis of electrical and electronic

equipmentwaste, finding that higher molecular weight polyaromatic hydrocarbons (PAHs) were thermally degraded via cracking when nickel catalysts were used. They formed smaller molecular weight aromatic compounds and hydrocarbon gases, increasing the hydrogen yield.Aboulet al. (Aboul et al., 2018)found that altering the iron metal ratio in the catalyst may adjust thetype and morphology of the deposited carbon.Here, hybrid materials, CNTs, carbon nanofibres (CNFs) accompanied withcarbon nano-onions (CNOs), as opposed to CNTs, were collected from intermediate iron loadings. Furthermore, compared with Ni catalysts,iron-based catalysts have generated higher carbon deposit yields because of the decent dispersion in thealuminium oxide(Al_2O_3) support material (Yao et al., 2018b). However, other studies have reported different results in which better dispersion was obtained using Ni-based catalysts, although lower carbon deposits or catalytic activity was observed(Liu et al., 2017). Overall, the literature suggests that ironexhibits better catalytic activity than other transition metals in the thermal catalytic degradation of plastic waste. Additionally, compared with Ni and other metals, iron is a cost-effective metal thatis a relatively more suitable candidatefor the catalytic pyrolysisof plastics waste and large-scale applications(Panda et al., 2010).

Support materials also play an important role in catalyst properties;they promote the dispersion of active metal particles and provide mass transport channels and reaction sites as a result of their physicochemical structure(Deelen et al., 2019). In general, several types of materials have beenused as supports, including metal oxides (Aboul et al., 2018; Torres et al., 2014), non-metallic oxides (Shen & Lua et al., 2015; Wei et al.,

2001), molecular sieves (López et al., 2011; Santos et al., 2018) and biochar (Li et al., 2020a; Zhang et al., 2019) from the pyrolysis of biomass. Li et al. (Li et al., 2014)found that more uniform carbon materials were obtained from alumina as opposed to zeolite-supported catalysts because of their porous structure. Yao et al. (Yao et al., 2018b)observed that alumina supports exhibited better effects, and the catalytic results changed with the formation of various crystalline phases.However, Santos et al. (Santos et al., 2018) discovered that support materials with many mesopores inhibited the conversion of volatiles to solid products.Takenaka et al. (Takenaka et al., 2001) obtained highlyunusual results;they reported that the catalytic support silica, without a pore structure, was the most satisfactory catalyst in terms of carbon deposit. This may be indicative of the relatively week affect the physical structure of the support hadon the catalytic process. These studies indicate that selecting different supporting materials may adjustthe distribution and quality of products, particularly for gaseous or carbon deposits.However,these studies rarely consideredliquid oil during catalytic pyrolysis of plastic waste, andthere is uncertainty as to the mechanism underlying the competitive transformation between products. The conversion mechanism of plastic waste using different support materials also requires further investigation.

This study utilised four types of materials, Al_2O_3, silicon dioxide (SiO_2),titanium dioxide (TiO_2), and ZSM-5,as supports for iron catalysts, and polypropylene (PP) waste was selected as the raw material. The effect of supports onthe catalytic pyrolysisof plastic waste, correlation of support with catalyst activity, and properties of products were exploredbased on thephysicochemical properties of

fresh catalysts and obtained products. An in-depth analysis of the related reaction mechanisms was also undertakenconcurrently.

2 Materials and methods

2.1 Materials

The PP samples were collected from a waste lunch box (washed);**Table S1**details the corresponding proximate and ultimate analyses.The ultimate analysis showed that carbon and hydrogen make up approximately 99 wt.% of the raw materials. The proximate analysis showed that the raw materials were abundant in volatiles (up to 99.87 wt.%),with only 0.06 wt.% ash.

Iron nitrate nonahydrate ($Fe(NO_3)_3 \cdot 9H_2O$, ≥98.50%), Al_2O_3(≥99.99%), SiO_2 (≥99.7%), and TiO_2(≥99.50%) were purchased from Sigma-Aldrich (China). Absolute ethanol (≥99.7%)was purchased from Sinopharm Chemical Reagent Co., Ltd. (China).ZSM-5(SiO_2/Al_2O_3 ratio=23)was purchased from Tianjin Nanhua Catalyst Co., Ltd. (China). All other chemicals were of analytical grade and used without further purification. The catalysts used in this study were prepared using an impregnation method, as described in previous studies (Cai et al., 2020a; Cai et al., 2020b);10 wt.% iron was introduced in the catalysts. For the Fe/Al_2O_3 catalyst, 0.72 g $FeNO_3 \cdot 9H_2O$ was dissolved in 30 mL absolute ethyl alcohol. Following completedissolution, 0.9 g Al_2O_3 was added to the solution and stirred at 50 °C with a magnetic stirrer until the solution had formed a slurry. The slurry was oven-dried at 105 °C for 12 h to remove excess ethanol. The obtained solid was smashed into small particles between 0.08 and

0.16 mm. The catalyst powder sample was calcined at 800°C for 2 h at a heating rate of 20 °C min^{-1} in air. After cooling to room temperature (~25°C) naturally, the catalyst was collected and labelled as Fe/Al_2O_3. The other three catalysts, using SiO_2, TiO_2, and ZSM-5 as support materials, were prepared using the same method and ratio, and were termed asFe/SiO_2, Fe/TiO_2, and$Fe/ZSM-5$, respectively.

2.2 Catalytic pyrolysis experiment

Catalytic pyrolysis experiments were conducted in a two-stage fixed-bed reactor (**Fig. S1**). For each trial, an iron-based catalyst (0.5 g) was placed into a quartz bracketplantloaded on the lower catalytic stage. Then,nitrogen was introduced into the reactor to create an inert atmosphereat 500 $mLmin^{-1}$ for 20 min. Subsequently, thenitrogen gas flow velocity was switched to 100 $mLmin^{-1}$, and the lower stage was first preheated to 800°C from the indoor temperature at a heating rate of 20°C min^{-1} and maintained at isothermal. As soon as the lower stage reached 800 °C,a hanging quartz basket with 1 g of plastic waste inside was introduced into the upper stage using a telescopic device. The upper pyrolysis stage wasconcurrently heated at a rate of 10 °Cmin^{-1} to 500 °Cand maintained at isothermal for 10 minprior to completing the catalytic pyrolysis experiments. To adequately collect the products, liquid oil and gaseous products were collected separately from repeated trials(Tang et al., 2020). Volatiles from catalytic pyrolysis wereliquefied using liquid nitrogen, and liquid oil was collected once the condensing bottle temperature returned to room temperature. For gaseous products, ice water was used to condense the volatiles to avoid the

146 excessive condensation of small molecules; this resulted in an incomplete collection.
147 The specific collection method was that: when upper pyrolysistemperature reached
148 300°C, the gas collecting bag was connected with the end of the gas path for 30 min
149 for gas collection.The black solid residue in the lower quartz bracket was
150 gatheredwhen the entire reaction system was cooled to room temperature (~25 °C).
151 Notably, the gaseous yield was determined from the total gas volume, gas density,
152 and gas volumeafter nitrogen was removed (Zou et al., 2018). The liquid oil yield was
153 calculated from the difference betweenthe initial and final weights of the condensate
154 bottle in the liquid nitrogen condenser. For the solid product, yield was computed
155 using the weight difference of the quartz holderbefore and after the catalytic pyrolysis.
156 Furthermore, the experiment using the same catalyst was carried out at least three
157 times, and the average was computed from three sets of data with an error<5%.

158 **2.3 Characterisation of catalyst and catalytic pyrolysis products**

159 X-ray diffraction (XRD) (Philips X'Pert PRO, Japan) was used to explore the
160 crystalline structures of the prepared catalysts;the scanning range and speed were
161 10–80° and 7° min^{-1}, respectively. The physical structure was determinedusing nitrogen
162 adsorption measurements (Quantachrome IQ, USA) at -196 °C. The specific surface
163 areas werecalculated using the Brunauer–Emmett–Teller (BET) method andpore size
164 distribution was computed using the non-linear density function theory(NLDFT)
165 calculation modelwith the adsorption branch.Moreover, total pore volume (V_{total})was
166 calculated from the maximum P/P_0, and the average pore diameter was determined

using the V_{total} and specific surface areas.

Gaseous products were detectedusinggas chromatography (GC) (Panna A91, China). Two different modules, a thermal conductivity detector (TCD) and flame ionisation detector (FID), were equipped to separate and analyse as many chemical species as possible in these gaseous products. The relative volumetric yields of other gaseous compounds were calculated, with the exception of the nitrogen inside. Furthermore, the lower heating value(LHV) of the gaseous products was computed using Eq. (1):

$$LHV(MJ/Nm^3)=0.126\times CO+0.108\times H_2+0.358\times CH_4+0.665\times C_nH_m \quad (1)$$

where each species represents itsvolumetric fraction.

The components of the liquid oil were identified using GC-mass spectroscopy (GC-MS, Agilent, HP7890 series GC with an HP5975MS detector, United States) with an HP-5MD capillary column that had a temperature limitation between 0 and 350 °C. The organic components in liquid oil were identified using a mass spectral library(NIST14.L).

Transmission electron microscopy (TEM) and high-resolution transmission electron microscopy (HR-TEM) were used to visualisethe surface morphology and size of the reacted catalysts with a field-emission transmission electron microscope (FE-TEM; TecnaiG2 F20 S-TWIN, United States), at an accelerating voltage of 200 kV. Using the XRD results, the size of the carbon and ironin the reacted catalysts (D_C and D_{Fe}) were calculated usingthe Scherrer equation (Eq. (2)) based on the (002) and (110) peaks, respectively. The interlayer spacing (d_{002}) of carbon was calculated using Brag's law, as shown in Eq. (3). The graphitisation degree (g^d) and the number of carbon layers (N)

were evaluated based on the interlayer spacing.Thermogravimetric analysis (TGA) was carried out for the reacted catalyst at a heating rate of 20 °C min^{-1}on a DiamondTG/DTA (PerkinElmer Instruments,China) to analyse the carbon deposit properties. Furthermore, Raman spectra from 800 $cm^{-1}$to 3200 cm^{-1}were obtained to determine the graphitisation degree of the carbon deposits using aRaman instrument with an excitation wavelength of 532 nm (LabRAM HR 800, France):

$$D=k\lambda/\beta\cos\theta \quad (2)$$

$$d_{002}= n\lambda/2\sin\theta \quad (3)$$

3 Results and discussion

3.1 Prepared catalysts

The crystal properties of the fresh catalysts were studied using XRD, and the results arepresented in **Fig. 1a**. Several broad and weak peaks were observed for the Fe/Al_2O_3 catalyst, which were associated with the Al_2O_3support material. There was only one peak related to Fe_2O_3 at approximately 35.7°.The Fe/SiO_2 catalyst showed sharp and intense Fe_2O_3 diffraction peaks, indicating a high degree of crystallisation;a left peak located at approximately 25°was attributed to SiO_2. The XRD diffraction spectrum of Fe/ZSM-5 showed strong and narrow features and multiple peaks indicative of the crystalline phases of Fe_2O_3. There were also many dense peaks at relatively low angles; thisrepresents the characteristic peak of the ZSM-5 molecular sieve. Compared with the Fe/SiO_2 catalyst, there was a slight difference observed for the Fe/ZSM-5 catalyst, in which an Fe-Si bond was formed. For the Fe/TiO_2 catalyst,

the diffraction peaks were more numerous, higher, and sharper; however, most peaks were associated with TiO_2. Only one peak at approximately 35.7°was ascribed to the active component, Fe_2O_3.The crystalline phases of Fe_2O_3 prepared by impregnation were mainly alpha, and the corresponding PDF card number was 01-089-0598.By contrast, crystalline Fe_2O_3 and Fe_3O_4were obtained from bimetallic catalysts (Yao et al., 2021), reflecting the critical influence of the introduction of other metals.

Each supporting materialexhibiteddifferent dispersive capacities for the samemetal.**Table S2** details the average crystallite size of $Fe_2O_3$for all catalysts calculated using the Scherrer equation from the peak at approximately 2θ and 32.8°. The exact Fe_2O_3 average crystallite size was26.24, 37.53, 43.77 and 76.93 nm for the Fe/Al_2O_3, Fe/SiO_2,Fe/ZSM-5 and Fe/TiO_2catalysts, respectively. The results show that the iron catalyst was well-dispersed over theAl_2O_3 support, followed by the SiO_2, ZSM-5, and TiO_2 supports. Yao et al. (Yao et al., 2018b)found that iron can disperse well on an Al_2O_3 support, which plays a critical role in subsequent catalytic conversion; SiO_2 has also been widely used as a support material. However, better dispersion or a smaller ironparticle size was obtained in this study compared with a previous report(Liu et al., 2017).The larger crystallite sizesobtained fromTiO_2 supportmaterials have also been observed in other studies; these larger sizes have caused relatively lower catalytic activity(Rossetti et al., 2013).

The nitrogen isothermal adsorption–desorption curves and pore size distribution of all prepared catalysts are shown in the insets of **Fig. 1b** and **Fig. 1b**, respectively. **Fig. 1b** shows that the Fe/Al_2O_3 and Fe/SiO_2 catalysts exhibitedtype III isotherms and H3

hysteresis loops(at relativelyhigher pressures of approximately 0.5–1.0). This is characteristic of slit holes formed from the accumulation of flake particles,often observed in mesoporous or macroporousmaterials(Tsai et al., 2002);evidently, the pore size of $Fe/SiO_2$was slightly larger. In addition, for the isotherms of Fe/ZSM-5, the volumetric absorption was higher at relatively low P/P_0; this is related to the presence of micropores. **Table S2** presents the pore structural parameters, such as specific surface area, pore volume, and average pore diameter. The Fe/ZSM-5 catalysthad the maximum S_{BET} and minimum $D_{average}$, corresponding to 178 m^2 g^{-1} and 5.01 nm, respectively. This originates from the porous characteristics of the ZSM-5substrate.The highest V_{total} and$D_{average}$were obtained from Fe/SiO_2catalyst, being 1.11 cm^3g^{-1} and 46 nm, respectively. Notably, the Fe/TiO_2 catalyst had a relatively lowerS_{BET} and V_{total}, which may be due to the poor dispersity and larger iron oxide. The inset in**Fig. 1b** shows the pore size distributions of the four catalysts according to the QSDFT model. A clearraised peak at approximately 28 nm was observed for Fe/SiO_2, and there were no pores smaller than 10 nm; thiscontributed to the largest average pore diameters. For the Fe/ZSM-5 catalyst, there was a sharp peak at approximately 3 nm, indicative of the presence of small mesopores and the corresponding large S_{BET} of the Fe/ZSM-5 catalyst.These results were also consistent with theS_{BET} and $D_{average}$ values presented in **Table S2**.

3.2 Analysis of yield and composition

3.2.1 Yield of catalytic pyrolysis products

Table 1 presents the product distributions of different phases from the catalytic pyrolysis of PPwaste.Without the catalyst, PP largely cracked into liquid oil (~46 wt.%)and gaseous products(~45 wt.%);the remaining coke was negligible.Oncethe catalyst was added, the yield of solid carbon depositsemerged;a dramatic decrease in the liquid oil yield was also observed. For the Fe/Al_2O_3 catalyst, a higher solid (30.2 wt.%) and lower gaseous (41.7 wt.%) yield was observed.A greater amount of liquid oil (20.6 wt.%) was collected forthe Fe/ZSM-5 catalyst;this may be related to a smaller pore size that limits the catalytic reaction or the intrinsic acidity of the ZSM-5 support that promotes the formation of aromatic hydrocarbons(Che et al., 2019).

For the Fe/SiO_2 catalyst, a lower yield of the liquid product was obtained. This might be attributed to the fact that large molecules could enter the larger pores of the Fe/SiO_2 catalyst andcome into contact with active sites, which is beneficial to the further cracking of volatiles(Hamid et al., 2017).A lower solid (26 wt.%) and higher gaseous product (45.7 wt.%) yield was obtainedfor Fe/TiO_2.The excessively strong interaction between iron species and TiO_2 may lower the reduction of iron oxide particles, decreasing catalyticactivityduring the catalytic pyrolysis(Rossetti et al., 2013). Notably, the gaseous productyield was more stable than the other two products, which may reflect the potential conversion pathway.This pathway is characterised by larger molecules in liquid oil being involved in the cracking and deposition process, largely

converting into carbon deposits and producing a lower liquid oil yield. Furthermore, the mass balance for the PP catalytic pyrolysis was approximately 90 wt.%, and 10% errors may be related to the pyrolysis volatiles condensed on the inner walls of the reactor or specific hydrocarbon gases that are difficult to detect with GC.

3.2.2 Components of gaseous products

The gaseous product distribution of the catalytic pyrolysis plasticwaste is presented in **Table 1**. Apparently, hydrogen gas (H_2),alkane (like CH_4), and olefin gases (e.g., C_2H_4)were dominant in the gaseous form.**Table 1** shows that without the catalyst, CH_4 was the main component, accountingfor >54 vol.% of gaseous products.Subsequently, H_2 and C_2H_4 occupied 22.8 vol.% and 20.5 vol.%, respectively. However, more H_2 was collected from gasification process (Liu et al., 2019). In addition, a small amount of C_{3+}, including propylene and propane, were also observed. At high temperatures, PP crackedtoolefins (including ethylene)in a random scission manner, and further crackedinto C_2H_4, CH_4, and H_2(Chi et al., 2018).Withthe introduction of a catalyst, the gaseous composition greatly altered with a significant decrease in CH_4 and C_2H_4;however, the proportion of H_2 increased significantly, and some carbon monoxide (CO)was detected. The increase in H_2may be attributed to the secondary reaction of hydrocarbon gases on the surface of the catalyst, while the CO produced may be related to the presence ofFe_2O_3. Under the pyrolysis atmosphere, Fe_2O_3 was reduced to iron by H_2 or other hydrocarbons,and oxygen was possibly released in the form of H_2O; thismay be further transferred to CO by reacting with hydrocarbons(Zhang et al.,

293 2015).

294 Furthermore, the gaseous component distribution differedas a function of the
295 catalysts with various supports.The H_2 content increased by 157% in the presence ofthe
296 Al_2O_3support catalyst compared to that in the absence of the catalyst;specifically, the
297 H_2yield increased from 22.8 vol.%to 58.7 vol.%withthe introduction of the Fe/Al_2O_3
298 catalyst.Hydrogenis mainly generated from the cracking of C-H bonds in hydrocarbons,
299 particularly with small molecules of hydrocarbons such as CH_4 and C_2H_4,resulting in a
300 sharp decrease in CH_4 and C_2H_4(Barbarias et al., 2018). The othercatalysts (Fe/SiO_2,
301 Fe/TiO_2, and Fe/ZSM-5) had similar methaneyields (~42 vol.%). However, the Fe/TiO_2
302 catalyst produceda higher volumetric fraction of $C_2H_4$and a lower volumetric fraction
303 of H_2; this means that there was less C_2H_4involved in the catalytic depositionin the
304 presence of the Fe/TiO_2 catalyst. This reflects the relatively low activity of the Fe/TiO_2
305 catalyst, whichmay be associated with the low specific surface areas and
306 underdeveloped pores of the Fe/TiO_2 catalyst.**Table 1** shows that the hydrogen
307 production trend was similar to the solid product yield, further confirming that
308 hydrogen is mainly formed from solid deposition.

309 **Table 1** also presents the LHV of gaseous products derived fromthe catalytic
310 pyrolysisof PP. The LHV of gaseous products from pure PP pyrolysiswas as high as
311 36.8 MJ Nm^{-3}; this is comparable to that of the natural gas(Tang et al., 2019). The
312 results show that the LHV of gases from different catalysts varied from 21.2 MJ Nm^{-3} to
313 26.9 MJ Nm^{-3};these values werelower than that obtained without catalysts; however,
314 the gases can still can be used as industrial fuel.

3.2.3 Components of liquid oil

Fig. 2and **S2** illustrate the carbon number distribution (relative percentage of peak area) andchromatograms, respectively,for organic constituents in liquid oil collected using different catalystsduringthe catalytic pyrolysis. The liquid oil from PP pyrolysis in the absence of thecatalyst contained a large number of aromatic hydrocarbons; these aromatics had a wide range of carbon number, which varied from C6 to C22.This wide range maybe attributed to the formation of aromatics from the olefins derived from PP pyrolysis via the Diels–Alder reaction and dehydrogenation at high temperatures (600–800°C) (Park et al., 2019a). The specific ingredients of the liquid productswere relatively complex, varying from monocyclic aromatic hydrocarbons to PAHs, such as benzo[e]pyrene. To obtaindetailed information on the composition of the liquid oil, the peak area percentage was used to analyse the relative content of different components. **Fig. 2**shows that >14% benzene, toluene, and xylene (BTX) was directly producedfrom PP pyrolysis.The proportion of C10 was higher (20.8%) than that of any otheringredient; C10corresponded to 4-phenylbut-3-ene-1-yne. When the iron-based catalyst was introduced, greater changes were observed in the liquid components. For the liquid product from Fe/Al_2O_3 catalyst, BTX was barely detected, although the proportion of C12, C14, C16 and C20 was largely increased.The components in the catalytic pyrolysis liquid oiltended to occur in more stable forms without branches.For example, naphthalene was the main form of C12 in catalytic pyrolysis oil as opposed to 4-phenylbut-3-ene-1-yne. Naphthalenemay be produced from monocyclic aromatics, 4-Phenylbut-3-ene-1-yne,or long chain olefins(Carlson et

al., 2009). Furthermore, naphthalene may also be generated from the break of branched chains in 2-methyl naphthalene. Compared with theliquid oil composition obtained using the Fe/Al_2O_3 catalyst, the use of Fe/SiO_2resulted in a similar liquid oil composition. However,xylene could continue to be collected and this may also reflect aweaker catalytic activity of Fe/SiO_2 compared to that of the Fe/Al_2O_3 catalyst.In comparison to other catalysts, the liquid oil obtained when Fe/ZSM-5was used exhibitedricher compositions,which may berelated to the intrinsic surface acid sites on ZSM-5(Che et al., 2019). The presence of acid sites contributes to the formation of aromatics andis significantly conducive to forming carbon deposits; this mayconstitute the major source of amorphous carbon(Chen et al., 2019). For theFe/TiO_2 catalyst,PAHs(such as C16 and C20, corresponding to pyrene and benzo[e]pyrene, respectively) showed an apparent increase in liquid oil;these macromolecules are considered to be the precursors during carbon depositsformation (Park et al., 2019b).The increase in PAH content may be due to thelow specific surface area and underdeveloped pores of the TiO_2 support. Notably, liquid oil is abundant inaromatics with carbon numbers between 8 and 16, which means it is feasible as anadditivefor jet fuel.(Zhang et al., 2019). The liquid oil may also be used as a raw material to prepare other chemical products through refinement(Wang et al., 2020b; Xu et al., 2020; Yuan et al., 2021).

3.2.4 Components of reacted catalysts

Fig. 3 presents theTEM imageryand the outer diameter distribution of the CNTs in

the carbon deposits on reacted catalysts. The fibre-like carbon material and themetalnanoparticleson the inside were observed in all TEM images. TEM images ofthe reacted Fe/Al_2O_3catalyst in **Fig.3a** confirm thatirregular, convoluted, and intertwined multiwall CNTs were prepared.The lattice fringe of nanoparticles on the inside was 0.204 nm, corresponding to the (110) plane of iron (**Fig. 3a** inset). **Fig.3b** shows that the outer diameter distribution of CNTsobtained using the Fe/Al_2O_3 catalyst was between 10 nm and 30 nm. Although the ratio of the standard deviation to the average outer diameter exceeded 10%,the size of CNTs was more uniform than that previously reported(Gong et al., 2012; Jia et al., 2020; Yao et al., 2018a). This can be attributed to the improved dispersion of active iron species in the Al_2O_3 support.This better dispersion is beneficial to obtaina more uniform size of CNTs, although it may also lead to entangled CNTs. For carbon deposits from the Fe/SiO_2 catalyst (**Fig.3c**), a large number of silica nanoparticleswere clustered together, and CNTswere away from each other withoutbeing interwoven; thismay be attributed to the improved dispersion and lower concentration per m^2 of iron(Rossetti et al., 2013). The combination of these two phenomena eventually led to an independent and uniform distribution of CNTs. A small number of defects produced from the thermochemical processwere also observed at the edge of the tube wall (**Fig. 3c** inset). The size of the produced CNTs washomogeneous, and the outer diameter of the CNTs was between 25 nm and 34 nm, with a very small standard deviation (1.8 nm) (**Fig. 3d**).Based on the TEM results, SiO_2may be a suitable support to preparenon-interlaced CNTs.Furthermore, clear bamboo-like structures were observed for CNTswith some complete and some

incomplete knots inside; this may be attributed to the continuous deformation of metal particles and the restoration of cohesive forces(Lin et al., 2007).

In terms of thecarbon deposited from Fe/ZSM-5(**Fig. 3e**),more uneven and chaotic CNFmaterialwas observed; it included tubes and fibres, which may be attributed tosmaller pore sizes or narrower channels (Li et al., 2014). It is also possible that structural collapse due to thermal instability at high temperatures resulted in the uneven dispersion and instability of metal particles, leading to diverse carbon deposits. The diameters of the CNF materials are presented in**Fig. 3f**;they weresignificantly differentfrom each other.Furthermore, TEM images of the reacted Fe/TiO_2catalyst (**Fig.3g**) showed a completely different type of carbon material from the other catalysts; this wasa CNF-like chainwith irregular iron particles within every shot of the chain.The carbon fibrewas twisted like fried dough twist,which did not resemble CNTs.As the active metal component was continuously stretched and deformed during the growth of graphene while being impacted by its own stress and reciprocation, the small metal particles were separated (Lin et al., 2007). The distribution of the outer diameter was wider ornon-uniform(**Fig. 3h**). Overall,the poor dispersion of active iron produced larger metal particles, which negatively impacted the formation ofCNTs(Rossetti et al., 2013).These results demonstrate that various support catalysts havedifferent effects on the formation of carbon materials.Studies have reported that the vapour–liquid–solid (VLS) is the mechanism that forms CNTs during this process(Yao et al., 2020). This process firstinvolves the adsorption and decomposition of hydrocarbons into carbon atoms in the presence of iron nanoparticles. This is followed by the dissolution and

402 diffusion of carbon within the molten particles;ultimately, the carbon precipitates
403 fromthe particles and forms CNTs.

404 The reacted catalysts were evaluated using XRD to obtain information on the
405 crystals. **Fig.4a** shows that two peaks located at approximately 26 °and 44 °correspond
406 to carbon andiron, referring to PDF card numbers 01-075-1621 and 01-089-7194,
407 respectively. The other peaks for each catalyst were associated with the relevant
408 supports.Based on the XRD patterns, the crystallite size and some other parameters of
409 the CNTsand ironwere calculatedusingScherrer equation and Bragg's law(Major et al.,
410 2018), as shown in **Table 2**.In general, the half-peak width and the position of the
411 (002) carbon peakwere associated with the physical structure, such as the space of the
412 (002) peak and carbon layers of the formed CNTs. The interlayer space (d_{002}) for all
413 reacted catalysts wasslightly larger than the theoretical value (0.335 nm); this may be
414 attributed to defects produced during thecatalytic pyrolysis depositionprocess(Xia et
415 al., 2019). This was also evident in the TEM results shown in the inset of**Fig. 3c**. The
416 carbon layer thickness (Dc), based on the (002) peak, increased from 7.759nm to
417 11.365 nm, and the corresponding number of carbon layers was approximately
418 between 22 and 35; this means that the CNTs or fibres prepared were
419 multi-walled.The graphitisation degree of deposited carbon onthe reacted Fe/Al_2O_3,
420 Fe/SiO_2,and Fe/ZSM-5 catalysts increased from 0.36 to 0.374.Moreover, the
421 graphitisation degreeofthe carbon deposits on Fe/TiO_2increased up to 0.458; this
422 wasmuch higher than that recorded for the other catalysts. It has been reported
423 thatiron mayenhance the graphitisation degree of carbon materials(Xia et al.,

2020a).Therefore, the higher graphitisation degree of carbon from Fe/TiO_2may be related to the large number of ironparticles evident in the TEM results(**Fig. 3g)**. In addition, the average diameter of the reduced iron particles for different reacted catalysts was calculated; it varied from approximately 10.978 nm to 45.376 nm. Notably, the size of iron metal particles in different catalysts was inversely proportional to the corresponding solid yield (**Fig.4b**); thisindicates that large metal particles are unfavourable for carbon deposits.Larger particles have been reported to lead to a smaller active surface area,eventually leading to weaker catalytic properties (Jiang et al., 2009).In this study, it was found that a smaller active surface area may decrease the contact efficiency between volatile gasesand active metal particles, resulting in an inadequate reaction and a decrease in catalytic activity; thisleads to fewer carbon deposits. Moreover, the specific surface areas of catalysts, usually originating from support materials, also plays a non-negligible rolein the catalytic process (Kim et al., 2002). The Fe/TiO_2 catalysts, with lower specific surface areas, decreased the ability for mass transfer, leading toa lower contact efficiency andreduced carbon deposition yield. Other reports with different supports or active metals have also observed a close relationship between particle size and carbon deposit yields in Fig. 4b.

TGA was carried out to analyse the reacted catalysts (**Fig. 5**);**Fig. 5a** shows that when the temperature was <450 °C, the mass of all samples remained quite stable. With increasing temperature, the carbon on the reacted catalyst began to oxidise, and sample mass declined. When the temperature reached 750 °C, all carbon deposits on the

446 catalysts were completely oxidised, and mass remained stable. As such, although iron
447 was oxidised at higher temperatures, the effect of oxidation was less than 2%
448 compared with the reacted catalysts because of the lower loading. The results show
449 that the total weight losses were 37.95, 34.00, 32.54 and 27.60 wt.% for the reacted
450 Fe/Al_2O_3, Fe/SiO_2, Fe/ZSM-5 and Fe/TiO_2 catalysts, respectively.A larger (smaller)
451 weight loss was observed for the reacted Fe/Al_2O_3(Fe/TiO_2) catalyst; this is consistent
452 with the product distribution in **Table 1**. According to previous studies, different types
453 of carbon depositswere obtained during catalytic pyrolysis, and the TGA test may be
454 used to distinguish the types of carbon according to the oxidising temperature(Yang et
455 al., 2015). **Fig. 5a** shows thatthe maximum oxidation rate of the carbon deposits was
456 observed at approximately 650 °C.Therefore, 650 °C was selected as the boundary
457 temperature to distinguish between amorphous carbon and graphite. The weight loss
458 that occurred between 450 °C and650 °C was related to amorphous carbon on the
459 surface of the catalyst, and weight loss at higher temperatures corresponded to graphite.
460 **Fig. 5b** shows thatthe reacted Fe/Al_2O_3 catalyst had a higher proportion of graphite
461 carbon (~76%), suggesting the production of a filamentous carbon with higher thermal
462 stability (Yao et al., 2018b).However, for carbon deposits from the Fe/SiO_2, Fe/ZSM-5,
463 and Fe/TiO_2 catalysts, a higher proportion of amorphous carbon (over 50%)
464 wasobserved. The observation ofmore amorphous carbon materials may be related to
465 the relatively low catalytic activity of the ironparticles inside, leading to the formation
466 of amorphous carbon. Furthermore, the collected amorphous carbon may originate
467 from the oligomerisation of polycyclic aromatics(Deng et al., 2015).

To further explore the characteristics of the deposited carbon obtained, Raman spectroscopy was used to identify the graphitisation degree of carbon and the purity of CNTs.**Fig.6** shows three peaks at approximately 1340 cm^{-1} (D band), 1580 cm^{-1} (G band), and 2670 cm^{-1} (G' band), corresponding to the sp^3 disordered and defected in graphene, planar motion of sp^2-hybridised carbon atoms in graphite layers, and graphene-like sheets or CNTs, respectively(Dresselhaus et al., 2010; Malard et al., 2009). Furthermore, the intensity ratio of D to G bands (I_D/I_G) was used to estimate the number of disordered and defective sites in the carbon structure, andthe intensity ratio of G' and G bands ($I_{G'}/I_G$) was used to describe the purity of CNTs in the carbon deposits (Yao et al., 2017).**Fig.6a** shows that the I_D/I_Gratios of carbon deposits on the reacted Fe/Al_2O_3, Fe/SiO_2, Fe/ZSM-5, and Fe/TiO_2catalysts were 0.47, 0.55, 0.66, and 0.52, respectively; theseare comparable with those of the CNTs deposited from commercial catalysts in other studies(Awadallah et al., 2014).A slight decrease in the graphitisation degree was observed in the order of: Fe/Al_2O_3>Fe/SiO_2>Fe/ZSM-5 catalysts. Forthe Fe/TiO_2 catalyst, the graphitisation degree showed the opposite variation tendency;ahigher graphitisation degree was observed for reacted Fe/TiO_2, which may be related to the widespread presence of iron particles in the carbon materials (Xia et al., 2020b). Based on the$I_{G'}/I_G$ ratio,the carbon deposited on the Fe/Al_2O_3 catalysthad a higher valuethan that for the other catalysts, suggesting a higher purity of the CNTs (Jonathan et al., 2016). This was also demonstrated by the TEM results,which showed that the carbon deposits obtained from the Fe/Al_2O_3 catalyst contained a greater number of CNTs than those obtained from the

490 othercatalysts.The carbon deposits on the reacted Fe/ZSM-5 and
491 Fe/TiO_2catalystsshared asimilar and lower $I_{G'}/I_G$ ratio, reflecting the lower purity of
492 CNTs; this may be related to widespread carbon fibresor thedeformed carbon
493 material(Wepasnick et al., 2010).

494 Moreover, the accurate purity of CNTs was assessed based on theD-band, G-band,
495 and G'-band peaks(DiLeo et al., 2007);the purity was evaluated from the ratio of I_D/I_G
496 to $I_{G'}/I_G$. **Fig. 6b** shows thataccording to the curve fit equations, the purity of different
497 samples was in accordance with the results mentioned in TGA test. Therefore, the
498 graphite carbon obtained in this study was assumed to be CNTs. CNTs obtained from
499 the Fe/Al_2O_3 catalyst exhibited a relatively higher purity, and there was no significant
500 difference between the purity (>65%) determined using the ratio ofI_D/I_G and $I_{G'}/I_G$.
501 However, for carbon deposits onthe Fe/TiO_2 catalyst, there was a gap between the
502 values calculated from the corresponding I_D/I_G and $I_{G'}/I_G$;the purity calculated from
503 I_D/I_G was much larger than that obtained from I_D/I_G. This may have been caused by the
504 impurities in the catalysts leading to the differences in the band intensities(Lehman et
505 al., 2011).In this study, the widespread presence of iron particles withinthe carbon
506 deposits from the Fe/TiO_2 catalyst dramatically promoted the corresponding
507 graphitisationdegree, which mayhave caused thisdifference.

508 **4 Conclusion**

509 Four different materials (Al_2O_3, SiO_2, ZSM-5, and TiO_2) with different physical
510 structures and metal dispersive capacities were used as iron-based catalyst supports for

511 the catalytic pyrolysis of PPwaste to produce high-value hydrogen, liquid fuel, and
512 CNT products. In the presence of catalysts, liquid oil was converted to carbon deposits
513 and lighter gaseous products such as hydrogen.The Al_2O_3 based catalyst produced
514 higher catalytic activity in terms of higher carbon deposits (30.2 wt.%) and hydrogen
515 yield (58.7 vol.%),due to the smaller iron particles. The moderate surface area and
516 pore size may also play a critical role during the thermal conversion process.More
517 dispersive and uniform CNTs were gathered from the Fe/SiO_2catalyst with a larger
518 pore size and volume. By contrast,the Fe/TiO_2catalyst preferentially producedcarbon
519 fibres twisted like fried dough twist because of the larger iron particles and a small
520 specific surface area.In addition, more liquid and CNFswere gathered fromthe
521 Fe/ZSM-5 catalyst, in which the liquid was abundant in aromatic hydrocarbons.
522 Notably, the carbon depositionyield from different catalysts was closely related to the
523 particle size of the reduced iron. These results show that supports are more than merely
524 an inert structural substrate and their properties may significantlyinfluence catalytic
525 performance.

526 Prior to realising the high-value utilisation of plastic waste, considerable research
527 needs to be conducted.Firstly, further exploration of the conversion mechanism from
528 plastic waste should provide guidance for improving themass and quality of the target
529 products. Moreover, realpilot-scale or scaled experimental research should be
530 conducted for industrial validation. Concurrent environmental and economic
531 assessments should also be seriouslyconsideredin the application of these processes.

Acknowledgement

The authors wish to express their sincere thanks for the financial support from the National Key Research and Development Program of China (2018YFC1901204), the National Natural Science Foundation of China (51861130362), China Postdoctoral Science Foundation (2018M640696) and the Foundation of the State Key Laboratory of Coal Combustion (FSKLCCB2001). The experiment was also assisted by the Analytical and Testing Center in Huazhong University of Science & Technology (http://atc.hust.edu.cn, Wuhan 430074 China). We would like to thank Editage (www.editage.cn) for English language editing.

Reference

Aboul, A., Awadallah A. Production of nanostructured carbon materials using Fe–Mo/MgO catalysts via mild catalytic pyrolysis of polyethylene waste. *Chem. Eng. J.*, **354**(2018), 802-816. https://doi.org/10.1016/j.cej.2018.08.046.

Aboul-Enein, A., Awadallah, A. Impact of Co/Mo ratio on the activity of CoMo/MgO catalyst for production of high-quality multi-walled carbon nanotubes from polyethylene waste. Materials Chemistry and Physics, 238(2019), 121879. https://doi.org/10.1016/j.matchemphys.2019.121879.

Acomb, J., Nahil M, Williams P. Thermal processing of plastics from waste electrical and electronic equipment for hydrogen production. *J. Anal. Appl. Pyrolysis.*, **103**(2013), 320-327. http://dx.doi.org/10.1016/j.jaap.2012.09.014.

Ahmed, S., Aitani A, Rahman F, Al-Dawood A, Al-Muhaish F. Decomposition of hydrocarbons to hydrogen and carbon. *Appl. Catal., A.*, **359**(2009), 1-24. https://doi.org/10.1016/j.apcata.2009.02.038.

Awadallah, A., Aboul-Enein A, Aboul-Gheit A. Effect of progressive Co loading on commercial Co–Mo/Al2O3 catalyst for natural gas decomposition to COx-free hydrogen production and carbon nanotubes. *Energy Convers. Manage.*, **77**(2014), 143-151. http://dx.doi.org/10.1016/j.enconman.2013.09.017.

Barbarias, I., Lopez G, Artetxe M, Arregi A, Bilbao J, Olazar M. Valorisation of different waste plastics by pyrolysis and in-line catalytic steam reforming for hydrogen production. *Energy Convers. Manage.*, **156**(2018), 575-584. https://doi.org/10.1016/j.enconman.2017.11.048.

Cai, N., Xia S, Zhang X, Meng Z, Bartocci P, Fantozzi F, Chen Y, Chen H, Williams P, Yang H. Preparation of Iron- and Nitrogen-Codoped Carbon Nanotubes from Waste Plastics Pyrolysis for the Oxygen Reduction Reaction. *ChemSusChem*, **13**(2020a), 938-944. http://dx.doi.org/10.1002/cssc.201903293.

Cai, N., Yang H, Zhang X, Xia S, Yao D, Bartocci P, Fantozzi F, Chen Y, Chen H, Williams P. Bimetallic carbon nanotube encapsulated Fe-Ni catalysts from fast pyrolysis of waste plastics and their oxygen reduction properties. *Waste*

571 *Manag.*, **109**(2020b), 119-126. https://doi.org/10.1016/j.wasman.2020.05.003.
572 Carlson, T., Jae J, Huber G. Mechanistic Insights from Isotopic Studies of Glucose
573 Conversion to Aromatics Over ZSM-5. *ChemCatChem*, **1**(2009), 107-110.
574 http://dx.doi.org/10.1002/cctc.200900130.
575 Che, Q., Yang M, Wang X, Yang Q, Williams L, Yang H, Zou J, Zeng K, Zhu Y, Chen
576 Y, Chen H. Influence of physicochemical properties of metal modified ZSM-5
577 catalyst on benzene, toluene and xylene production from biomass catalytic
578 pyrolysis. *Bioresour Technol*, **278**(2019), 248-254.
579 https://doi.org/10.1016/j.biortech.2019.01.081.
580 Chen, X., Che Q, Li S, Liu Z, Yang H, Chen Y, Wang X, Shao J, Chen H. Recent
581 developments in lignocellulosic biomass catalytic fast pyrolysis: Strategies for
582 the optimization of bio-oil quality and yield. *Fuel Process. Technol.*,
583 **196**(2019), 106180. https://doi.org/10.1016/j.fuproc.2019.106180.
584 Chi, Y., Xue J, Zhuo J, Zhang D, Liu M, Yao Q. Catalytic co-pyrolysis of cellulose
585 and polypropylene over all-silica mesoporous catalyst MCM-41 and
586 Al-MCM-41. *Sci Total Environ*, **633**(2018), 1105-1113.
587 https://doi.org/10.1016/j.scitotenv.2018.03.239.
588 Dai, L., Zhou, N, Lv, Y, Cheng, Y, Wang, Y, Liu, Y, Cobb, K, Chen, P, Lei, H, Ruan, R.
589 Chemical upcycling of waste polyolefinic plastics to low-carbon synthetic
590 naphtha for closing the plastic use loop. *Sci Total Environ*, **782**(2021), 146897.
591 https://doi.org/10.1016/j.scitotenv.2021.146897.
592 Deelen, T., Hernández C, Jong K. Control of metal-support interactions in
593 heterogeneous catalysts to enhance activity and selectivity. *Nature Catalysis*,
594 **2**(2019), 955–970. https://doi.org/10.1038/s41929-019-0364-x.
595 Deng, Q., Zhang X, Wang L, Zou J. Catalytic isomerization and oligomerization of
596 endo-dicyclopentadiene using alkali-treated hierarchical porous HZSM-5.
597 *Chem. Eng. Sci.*, **135**(2015), 540-546.
598 http://dx.doi.org/10.1016/j.ces.2014.08.060.
599 DiLeo, R., Landi B, Raffaelle R. . Purity assessment of multiwalled carbon nanotubes
600 by Raman spectroscopy. *J Appl Phys*, **101**(2007), 064307.

https://doi.org/10.1063/1.2712152.

Dresselhaus, M., Jorio A, Hofmann M, Dresselhaus G, Saito R. . Perspectives on carbon nanotubes and graphene Raman spectroscopy. *Nano Lett*, **10**(2010), 751-8. http://www.ncbi.nlm.nih.gov/pubmed/20085345.

Ellis, L., Rorrer, N, Sullivan, K, Otto, M, McGeehan, J, Román-Leshkov, Y, Wierckx, N, Beckham, G. Chemical and biological catalysis for plastics recycling and upcycling. *Nature Catalysis*, **4**(2021), 539-556. https://doi.org/10.1038/s41929-021-00648-4.

Geyer, R., Jambeck J, Law K. Production, use, and fate of all plastics ever made. *Sci. Adv.*, **3**(2017), 1-5. https://doi.org/10.1126/sciadv.1700782.

Gong, J., Liu J, Wan D, Chen X, Wen X, Mijowska E, Jiang Z, Wang Y, Tang T. Catalytic carbonization of polypropylene by the combined catalysis of activated carbon with Ni2O3 into carbon nanotubes and its mechanism. *Appl. Catal., A.*, **449**(2012), 112-120. http://dx.doi.org/10.1016/j.apcata.2012.09.028.

Hamid, Z., Azim A, Mouez F, Rehim S. Challenges on synthesis of carbon nanotubes from environmentally friendly green oil using pyrolysis technique. *J. Anal. Appl. Pyrolysis.*, **126**(2017), 218-229. http://dx.doi.org/10.1016/j.jaap.2017.06.005.

Huo, E., Lei H, Liu C, Zhang Y, Xin L, Zhao Y, Qian M, Zhang Q, Lin X, Wang C, Mateo W, Villota E, Ruan R. Jet fuel and hydrogen produced from waste plastics catalytic pyrolysis with activated carbon and MgO. *Sci Total Environ*, **727**(2020), 138411. https://doi.org/10.1016/j.scitotenv.2020.138411.

Jia, J., Veksha A, Lim T, Lisak G. In situ grown metallic nickel from X–Ni (X=La, Mg, Sr) oxides for converting plastics into carbon nanotubes: Influence of metal–support interaction. *J. Cleaner Prod.*, **258**(2020), 120633. https://doi.org/10.1016/j.jclepro.2020.120633.

Jiang, L., Hsu, A, Chu, D, Chen, R. Size-Dependent Activity of Palladium Nanoparticles for Oxygen Electroreduction in Alkaline Solutions. *Journal of The Electrochemical Society*, **156**(2009), B643.

https://doi.org/10.1149/1.3098478.

Jonathan, A., Wu C, Williams P. . The use of different metal catalysts for the simultaneous production of carbon nanotubes and hydrogen from pyrolysis of plastic feedstocks. *Appl. Catal. B: Environ.*, **180**(2016), 497-510. http://dx.doi.org/10.1016/j.apcatb.2015.06.054.

Kim, S. The catalytic oxidation of aromatic hydrocarbons over supported metal oxide. *Journal of Hazardous Materials*, **91**(2002), 285–299. https://doi.org/10.1016/S0304-3894(01)00396-X.

López, A., Marco I, Caballero B, Laresgoiti M, Adrados A, Aranzabal A. Catalytic pyrolysis of plastic wastes with two different types of catalysts: ZSM-5 zeolite and Red Mud. *Appl. Catal. B: Environ.*, **104**(2011), 211-219. http://dx.doi.org/10.1016/j.apcatb.2011.03.030.

Lehman, J., Terrones M, Mansfield E, Hurst K, Meunier V. Evaluating the characteristics of multiwall carbon nanotubes. *Carbon*, **49**(2011), 2581-2602. https://doi.org/10.1016/j.carbon.2011.03.028.

Li, C., Zhang C, Gholizadeh M, Hu X. Different reaction behaviours of light or heavy density polyethylene during the pyrolysis with biochar as the catalyst. *J Hazard Mater*, **399**(2020a), 123075. http://www.ncbi.nlm.nih.gov/pubmed/32544769.

Li, Q., Faramarzi A, Zhang S, Wang Y, Hu X, Gholizadeh M. Progress in catalytic pyrolysis of municipal solid waste. *Energy Convers. Manage.*, **226**(2020b), 113525. https://doi.org/10.1016/j.enconman.2020.113525.

Li, X., Zhu G, Qi S, Huang J, Yang B. Simultaneous production of hythane and carbon nanotubes via catalytic decomposition of methane with catalysts dispersed on porous supports. *Appl. Energy.*, **130**(2014), 846-852. http://dx.doi.org/10.1016/j.apenergy.2014.01.056.

Lin, M., Tan J, Boothroyd C, Loh K, Tok E, Foo Y. Dynamical Observation of Bamboo-like Carbon Nanotube Growth. *Nano Lett.*, **7**(2007), 2234-2238. https://doi.org/10.1021/nl070681x.

Liu, Q., Hu, C., Peng, B., Liu, C., Li, Z., Wu, K., Zhang, H., Xiao, R. High H2/CO

661 ratio syngas production from chemical looping co-gasification of biomass and
662 polyethylene with CaO/Fe2O3 oxygen carrier. *Energy Convers. Manage.*,
663 **199**(2019), 111951.
664 Liu, X., Zhang Y, Nahil M, Williams P, Wu C. Development of Ni- and Fe- based
665 catalysts with different metal particle sizes for the production of carbon
666 nanotubes and hydrogen from thermo-chemical conversion of waste plastics. *J.*
667 *Anal. Appl. Pyrolysis*, **125**(2017), 32-39.
668 http://dx.doi.org/10.1016/j.jaap.2017.05.001.
669 Major, I., Pin J, Behazin E, Rodriguez A, Misra M, Mohanty A. Graphitization of
670 Miscanthus grass biocarbon enhanced by in situ generated FeCo nanoparticles.
671 *Green Chem.*, **20**(2018), 2269-2278. https://doi.org/10.1039/c7gc03457a.
672 Malard, L., Pimenta M, Dresselhaus G, Dresselhaus M. Raman spectroscopy in
673 graphene. *Phys. Rep.*, **473**(2009), 51-87.
674 http://dx.doi.org/10.1016/j.physrep.2009.02.003.
675 Modekwe, H., Mamo, M, Moothi, K, Daramola, M. Effect of Different Catalyst
676 Supports on the Quality, Yield and Morphology of Carbon Nanotubes
677 Produced from Waste Polypropylene Plastics. Catalysts, 11(2021), 692.
678 https://doi.org/10.3390/catal11060692.
679 Nahil, M., Wu C, Williams P. Influence of metal addition to Ni-based catalysts for the
680 co-production of carbon nanotubes and hydrogen from the thermal processing
681 of waste polypropylene. *Fuel Process. Technol.*, **130**(2015), 46-53.
682 http://dx.doi.org/10.1016/j.fuproc.2014.09.022.
683 Panda, A., Singh, R, Mishra, D. Thermolysis of waste plastics to liquid fuelA suitable
684 method for plastic waste management and manufacture of value added
685 products—A world prospective. *Renewable and Sustainable Energy Reviews*,
686 **14**(2010), 233-248. https://doi.org/10.1016/j.rser.2009.07.005.
687 Park, K., Jeong Y, Guzelciftci B, Kim J. Characteristics of a new type continuous
688 two-stage pyrolysis of waste polyethylene. *Energy*, **166**(2019a), 343-351.
689 https://doi.org/10.1016/j.energy.2018.10.078.
690 Park, Y., Lee B, Lee H, Watanabe A, Jae J, Tsang Y, Kim Y. Co-feeding effect of waste

691 plastic films on the catalytic pyrolysis of Quercus variabilis over microporous
692 HZSM-5 and HY catalysts. *Chem. Eng. J.*, **378**(2019b), 122151.
693 https://doi.org/10.1016/j.cej.2019.122151.
694 Prata, J.C.S., A. L. P. Walker, T. R. Duarte, A. C. Rocha-Santos, T. COVID-19
695 Pandemic Repercussions on the Use and Management of Plastics. *Environ Sci*
696 *Technol*, **54**(2020), 7760-7765. https://dx.doi.org/10.1021/acs.est.0c02178.
697 Rossetti, I., Gallo A, Dal Santo V, Bianchi C, Nichele V, Signoretto M, Finocchio E,
698 Ramis G, DiMichele A. Nickel Catalysts Supported Over TiO2, SiO2and
699 ZrO2for the Steam Reforming of Glycerol. *ChemCatChem*, **5**(2013), 294-306.
700 http://dx.doi.org/10.1002/cctc.201200481.
701 Santos, B., Almeida D, Marques M, Henriques C. Petrochemical feedstock from
702 pyrolysis of waste polyethylene and polypropylene using different catalysts.
703 *Fuel*, **215**(2018), 515-521. https://doi.org/10.1016/j.fuel.2017.11.104.
704 Shen, Y., Lua, A. Synthesis of Ni and Ni–Cu supported on carbon nanotubes for
705 hydrogen and carbon production by catalytic decomposition of methane. *Appl.*
706 *Catal., B.*, **164**(2015), 61-69.
707 Takenaka, S., Ogihara H, Yamanaka I, Otsuka K. Decomposition of methane over
708 supported-Ni catalysts:effects of the supports on the catalytic lifetime. *Appl.*
709 *Catal., A*, **217** (2001), 101-110.
710 http://dx.doi.org/10.1016/S0926-860X(01)00593-2.
711 Tang, Z., Chen W, Chen Y, Yang H, Chen H. Co-pyrolysis of microalgae and plastic:
712 Characteristics and interaction effects. *Bioresour Technol*, **274**(2019), 145-152.
713 https://doi.org/10.1016/j.biortech.2018.11.083.
714 Tang, Z., Chen W, Hu J, Li S, Chen Y, Yang H, Chen H. Co-pyrolysis of microalgae
715 with low-density polyethylene (LDPE) for deoxygenation and denitrification.
716 *Bioresour Technol*, **311**(2020), 123502.
717 https://doi.org/10.1016/j.biortech.2020.123502.
718 Torres, D., Pinill, J, Lázaro M, Moliner R, Suelves I. Hydrogen and multiwall carbon
719 nanotubes production by catalytic decomposition of methane:
720 Thermogravimetric analysis and scaling-up of Fe–Mo catalysts. *Int. J.*

721 *Hydrogen Energy*, **39**(2014), 3698-3709.
722 http://dx.doi.org/10.1016/j.ijhydene.2013.12.127.
723 Tsai, W., Chen, H, Hsieh, M, Sun,H, Chien, S. Regeneration of spent bleaching earth
724 by pyrolysis in a rotary furnace. *Journal of Analytical and Applied Pyrolysis*,
725 **63**(2002), 157–170. https://doi.org/10.1016/S0165-2370(01)00150-4.
726 Wang, J., Jiang J, Meng X, Li M, Wang X, Pang S, Wang K, Sun Y, Zhong Z, Ruan R,
727 Ragauskas A. Promoting Aromatic Hydrocarbon Formation via Catalytic
728 Pyrolysis of Polycarbonate Wastes over Fe- and Ce-Loaded Aluminum Oxide
729 Catalysts. *Environ Sci Technol*(2020a).
730 https://dx.doi.org/10.1021/acs.est.0c00899.
731 Wang, S., Zhao S, Uzoejinwa B, Zheng A, Wang Q, Huang J, Abomohra A. A
732 state-of-the-art review on dual purpose seaweeds utilization for wastewater
733 treatment and crude bio-oil production. *Energy Convers. Manage.*, **222**(2020b),
734 113253. https://doi.org/10.1016/j.enconman.2020.113253.
735 Wei, Y., Eres G, Merkulov V, Lowndes D. Effect of catalyst film thickness on carbon
736 nanotube growth by selective area chemical vapor deposition. *Appl. Phys. Lett.*,
737 **8**(2001), 1394-1396. https://doi.org/10.1063/1.1354658.
738 Wepasnick, K., Smith B, Bitter J, Howard Fairbrother D. Chemical and structural
739 characterization of carbon nanotube surfaces. *Anal Bioanal Chem*, **396**(2010),
740 1003-14. http://www.ncbi.nlm.nih.gov/pubmed/20052581.
741 Williams, P. Hydrogen and Carbon Nanotubes from Pyrolysis-Catalysis of Waste
742 Plastics: A Review. *Waste Biomass Valorization*, **12**(2020), 1-28.
743 https://doi.org/10.1007/s12649-020-01054-w.
744 Xia, S., Cai N, Wu J, Xiao H, Hu J, Chen X, Chen Y, Yang H, Wang X, Chen H.
745 Synthesis and formation mechanism of biomass-based mesoporous graphitic
746 carbon. *Fuel Processing Technology*, **209**(2020a), 106543.
747 https://doi.org/10.1016/j.fuproc.2020.106543.
748 Xia, W., Tang J, Li J, Zhang S, Wu K, He J, Yamauchi Y. Defect-Rich Graphene
749 Nanomesh Produced by Thermal Exfoliation of Metal-Organic Frameworks
750 for the Oxygen Reduction Reaction. *Angew Chem Int Ed Engl*, **58**(2019),

13354-13359. http://www.ncbi.nlm.nih.gov/pubmed/31407475.

Xu, S., Cao B, Uzoejinwa B, Odey E, Wang S, Shang H, Li C, Hu Y, Wang Q, Nwakaire J. Synergistic effects of catalytic co-pyrolysis of macroalgae with waste plastics. *Process Saf. Environ. Prot.*, **137**(2020), 34-48. https://doi.org/10.1016/j.psep.2020.02.001.

Yang, R., Chuang K, Wey M. Effects of Nickel Species on Ni/Al2O3 Catalysts in Carbon Nanotube and Hydrogen Production by Waste Plastic Gasification: Bench- and Pilot-Scale Tests. *Energy Fuels*, **29**(2015), 8178-8187. https://doi.org/10.1021/acs.energyfuels.5b01866.

Yao, D., Wang C. Pyrolysis and in-line catalytic decomposition of polypropylene to carbon nanomaterials and hydrogen over Fe- and Ni-based catalysts. *Appl. Energy*, **265**(2020), 114819. https://doi.org/10.1016/j.apenergy.2020.114819.

Yao, D., Wu C, Yang H, Zhang Y, Nahil M, Chen Y, Williams P. Chen H. Co-production of hydrogen and carbon nanotubes from catalytic pyrolysis of waste plastics on Ni-Fe bimetallic catalyst. *Energy Convers. Manage.*, **148**(2017), 692-700. http://dx.doi.org/10.1016/j.enconman.2017.06.012.

Yao, D., Yang H, Chen H, Williams P. Co-precipitation, impregnation and so-gel preparation of Ni catalysts for pyrolysis-catalytic steam reforming of waste plastics. *Appl. Catal. B: Environ.*, **239**(2018a), 565-577. https://doi.org/10.1016/j.apcatb.2018.07.075.

Yao, D., Yang, H., Hu, Q., Chen, Y., Chen, H., Williams, Paul T. Carbon nanotubes from post-consumer waste plastics: Investigations into catalyst metal and support material characteristics. *Appl. Catal. B: Environ.*, **280**(2021), 119413. https://doi.org/10.1016/j.apcatb.2020.119413.

Yao, D., Zhang Y, Williams P, Yang H, Chen H. Co-production of hydrogen and carbon nanotubes from real-world waste plastics: Influence of catalyst composition and operational parameters. *Appl. Catal. B: Environ.*, **221**(2018b), 584-597. http://dx.doi.org/10.1016/j.apcatb.2017.09.035.

Yuan, C., El-Fatah Abomohra, A, Wang, S, Liu, Q, Zhao, S, Cao, B, Hu, X, Marrakchi, F, He, Z, Hu, Y. High-grade biofuel production from catalytic pyrolysis of

781 waste clay oil using modified activated seaweed carbon-based catalyst.
782 *Journal of Cleaner Production*, **313**(2021), 127928.
783 https://doi.org/10.1016/j.jclepro.2021.127928.
784 Zhang, Y., Duan D, Lei H, Villota E, Ruan R. Jet fuel production from waste plastics
785 via catalytic pyrolysis with activated carbons. *Appl. Energy*, **251**(2019),
786 113337. https://doi.org/10.1016/j.apenergy.2019.113337.
787 Zhang, Y., Wu C, Nahil M, Williams P. Pyrolysis–Catalytic Reforming/Gasification of
788 Waste Tires for Production of Carbon Nanotubes and Hydrogen. *Energy Fuels*,
789 **29**(2015), 3328-3334. https://doi.org/10.1021/acs.energyfuels.5b00408.
790 Zou, J., Oladipo J, Fu S, Al-Rahbi A, Yang H, Wu C, Cai N, Williams P, Chen H.
791 Hydrogen production from cellulose catalytic gasification on CeO2/Fe2O3
792 catalyst. *Energy Convers. Manage.*, **171**(2018), 241-248.
793 https://doi.org/10.1016/j.enconman.2018.05.104.

794
795

796 **Table 1** Product distribution and gaseous composition from different catalysts

	No catalyst	Fe/Al_2O_3	Fe/SiO_2	Fe/ZSM-5	Fe/TiO_2
Gas yield, wt.%	45.3 ± 1.0	41.7 ± 0.9	42.6 ± 1.3	42.9 ± 0.8	45.7 ± 1.5
Liquid yield, wt.%	46.1 ±1.4	18.1 ± 1.2	16.5 ±0.2	20.6 ± 1.3	19.6 ± 1.1
Solid yield, wt.%	-	30.2 ± 0.5	29.4 ± 0.3	28.2 ± 0.3	26.0 ± 0.2
Mass balance, wt.%	~ 91.4	~ 90	~ 88.5	~ 91.7	~ 91.3
Gas composition, vol.%					
H_2	22.8	58.7	45.2	45.3	40.8
CH_4	54.8	32.4	42.0	42.9	45.2
CO	0	4.2	5.5	4.4	5.4
C_2H_4	20.5	3.7	6.0	6.0	6.9
C_2H_6	1.8	0.7	1.0	0.9	1.0
C_{3+}	0.1	0.3	0.3	0.5	0.7
LHV of gaseous product,MJ Nm^{-3}	36.8	21.3	25.2	25.3	26.9

797
798

799 **Table 2.** Graphitisation of carbon deposits and iron particles from XRD for the reacted

800 catalysts

Sample	D_C (nm)	N	D_{Fe}(nm)	d_{002} (nm)	g^d
Fe/Al_2O_3	7.8 ± 0.2	23 ± 2	11.0 ± 0.4	0.344 ± 0.001	0.364 ± 0.003
Fe/SiO_2	10.3 ± 0.3	30 ± 2	22.7 ± 1.2	0.341 ± 0.001	0.374 ± 0.002
Fe/ZSM-5	11.4 ± 0.2	33 ± 3	34.0 ± 2.6	0.343 ± 0.001	0.360 ± 0.002
Fe/TiO_2	8.3 ± 0.1	24 ± 1	45.4 ± 2.4	0.340 ± 0.002	0.458 ± 0.003

801
802

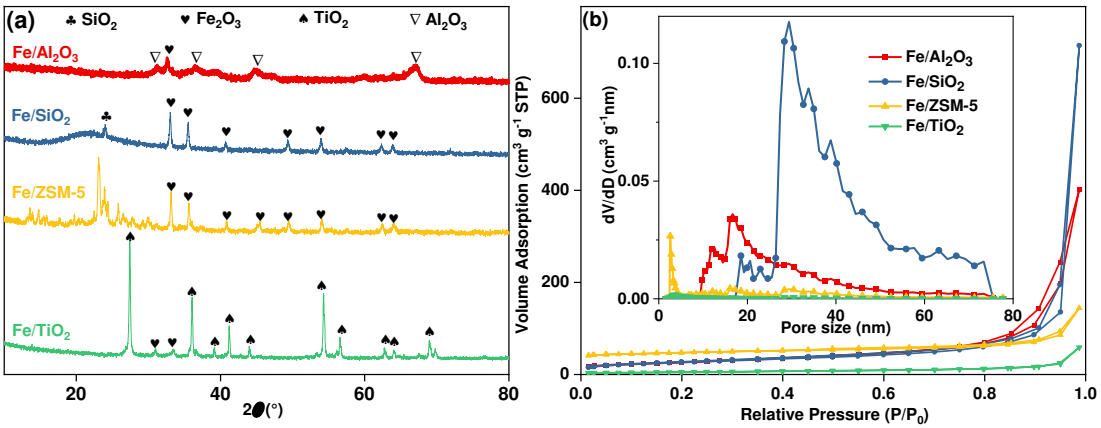

803

804 **Fig. 1**. Structural characterisation of prepared catalysts: (a) XRD diffraction patterns;

805 and (b) isothermal adsorption curve and pore size distribution.

806

807

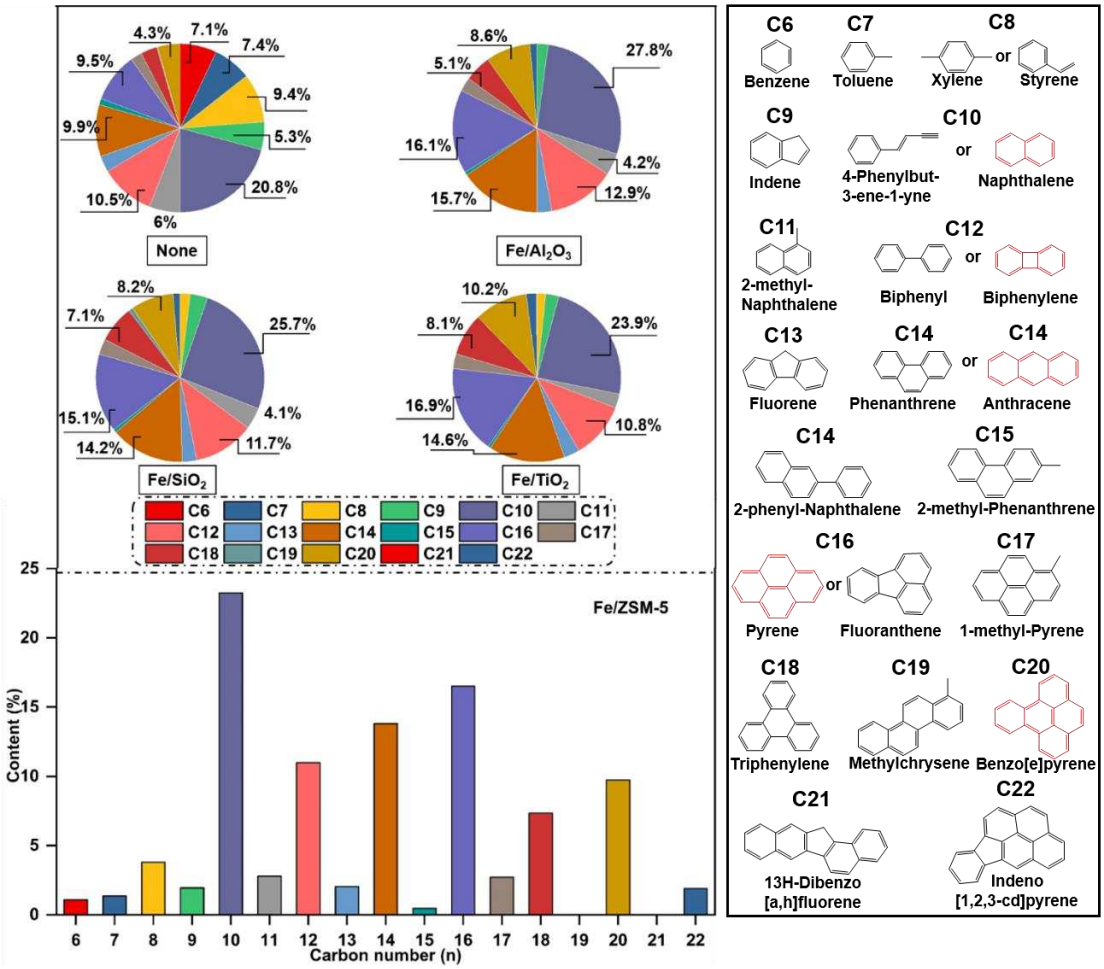

Fig. 2. Carbon number (% area) and the corresponding components of liquid products from the catalytic pyrolysis of PP waste in the presence of different catalysts.

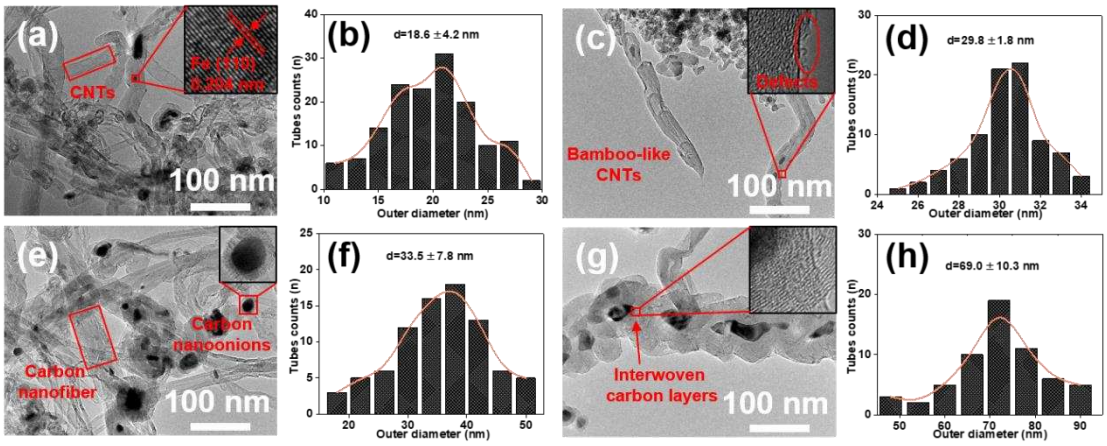

813

814 **Fig. 3**. TEM images of carbon deposits from catalytic pyrolysis PP waste: (a, b)

815 Fe/Al_2O_3; (c, d) Fe/SiO_2; (e, f) Fe/ZSM-5; and (g, h) Fe/TiO_2).

816

817

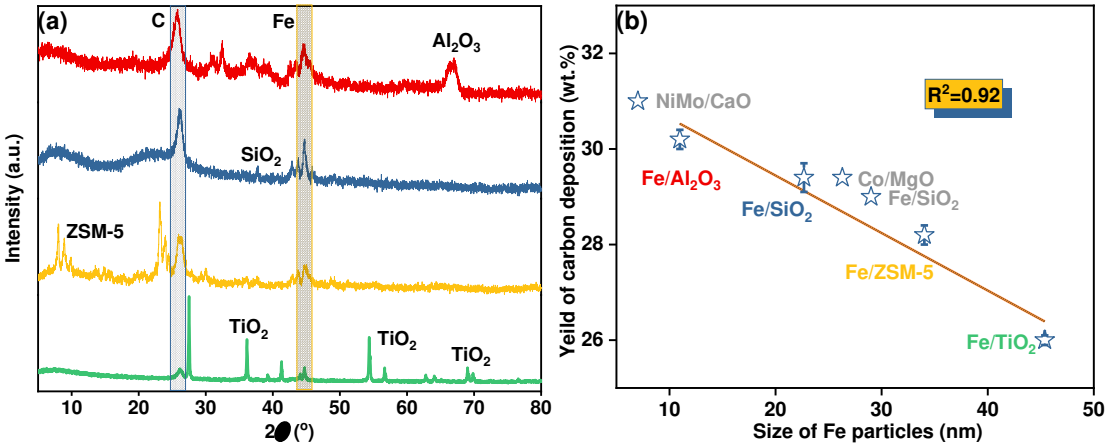

818

819 **Fig. 4.** (a) X-ray diffraction patterns of reacted catalysts; and (b) the association of

820 carbon deposit yields and the size of iron particles (comparisons: NiMo/CaO from

821 (Aboul-Enein et al., 2019), Co/MgO from (Modekwe et al., 2021) and Fe/SiO_2 from

822 (Liu et al., 2017).

823

824

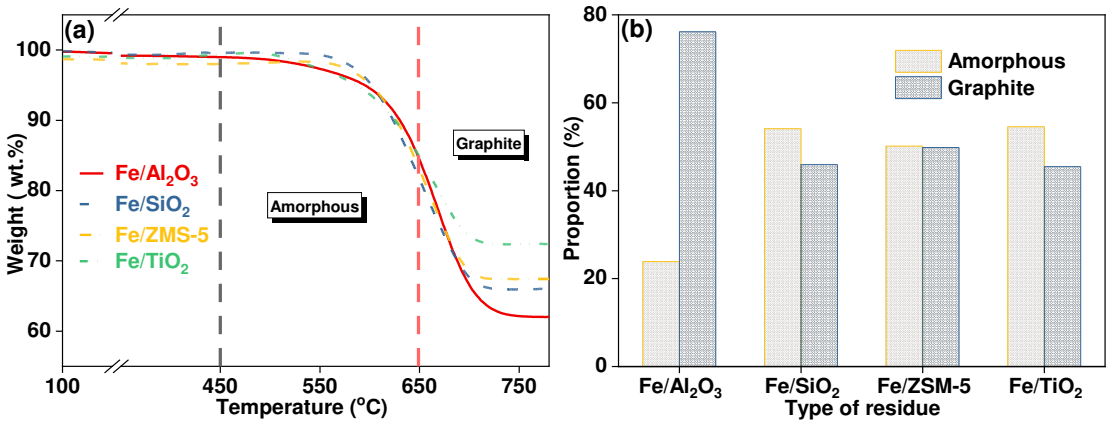

825

826

827 **Fig. 5**. (a) TG curves; and (b) proportion of different carbon types from carbon deposits

828 on the reacted catalysts.

829

830

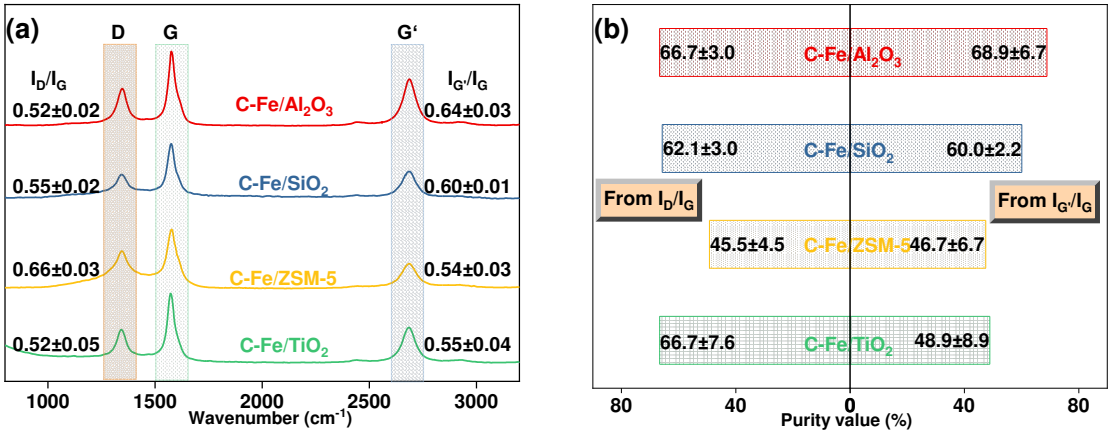

831

832

833 **Fig. 6**. (a) Raman spectra; and (b) purity of carbon deposits on the reacted catalysts.

834